Ångström-scale chemically powered motors

2014 EPL 106 30004

(http://iopscience.iop.org/0295-5075/106/3/30004)

epl A Letters Journal Exploring the Frontiers of Physics

May 2014

EPL, **106** (2014) 30004
doi: 10.1209/0295-5075/106/30004

www.epljournal.org

Ångström-scale chemically powered motors

Peter H. Colberg and Raymond Kapral

Chemical Physics Theory Group, Department of Chemistry, University of Toronto Toronto, Ontario M5S 3H6, Canada

received 13 February 2014; accepted in final form 24 April 2014
published online 15 May 2014

PACS 05.60.Cd – Classical transport
PACS 02.70.Ns – Molecular dynamics and particle methods
PACS 61.20.Ja – Computer simulation of liquid structure

Abstract – Like their larger micron-scale counterparts, Ångström-scale chemically self-propelled motors use asymmetric catalytic activity to produce self-generated concentration gradients that lead to directed motion. Unlike their micron-scale counterparts, the sizes of Ångström-scale motors are comparable to the solvent molecules in which they move, they are dominated by fluctuations, and they operate on very different time scales. These new features are studied using molecular dynamics simulations of small sphere dimer motors. We show that the ballistic regime is dominated by the thermal speed but the diffusion coefficients of these motors are orders of magnitude larger than inactive dimers. Such small motors may find applications in nano-confined systems or perhaps eventually in the cell.

Biological molecular motors operate under non-equilibrium conditions and consume fuel in their environment to drive conformational changes that enable them to carry out specific tasks. Motor proteins such as adenosine triphosphate synthase pump ions across the cell membrane, kinesin walks along microtubules to effect active transport in the cell, to name just two of the thousands of motors that contribute to the biological function of the cell [1]. These small molecular motors are able to perform their tasks in complex environments in spite of strong thermal fluctuations. Synthetic mimics of such molecular machines have been constructed [2–4]. On much larger micron scales, bacteria swim by using chemical fuel to drive various types of non-reciprocal conformational changes to produce directed motion [5].

Chemically powered synthetic motors that operate by phoretic mechanisms and do not rely on conformational changes for directed motion have been the subject of recent studies [6–9]. Metallic rod [10,11], Janus particle [12,13] and sphere dimer [14] motors with linear dimensions in the hundreds of nanometres and micron ranges have been extensively investigated and hold the promise of future applications, which include targeted cargo transport, controlled motion and stirring in microfluidic arrays, active self-assembly and directed chemical synthesis. Although such small motors are influenced by thermal fluctuations, continuum descriptions of phoretic motion [15–17] adequately describe the dynamics of such motors [12,18–21].

In this article, we consider the dynamics of even smaller Ångström-scale chemically powered motors with sizes of a few nanometres where new factors come into play. The motors are no longer much larger than the solvent molecules that comprise their environments. Consequently, solvent structure in the vicinity of the motor must be taken into account. Motors are subject to orientational fluctuations that tend to destroy ballistic motion. Since most potential applications utilize ballistic motion, the long reorientational times of mesoscale motors make directed motion easy to observe. For small Ångström-scale motors the reorientational times are very short. Straightforward application of macroscopic and hydrodynamic models to the dynamics is questionable or, at the very least, must be examined carefully. Nevertheless, it is well known that collective hydrodynamic modes play a crucial part in molecular-level dynamics, an example being the long-time tail in the velocity autocorrelation function [22]. Finally, fluctuations play an even more dominant role for these small motors than for larger mesoscale motors. Thus, the investigation of the dynamics of molecular-scale motors is both interesting and presents fundamental challenges.

Additional stimulus for such research is provided by potential applications of synthetic motors inside the cell or in

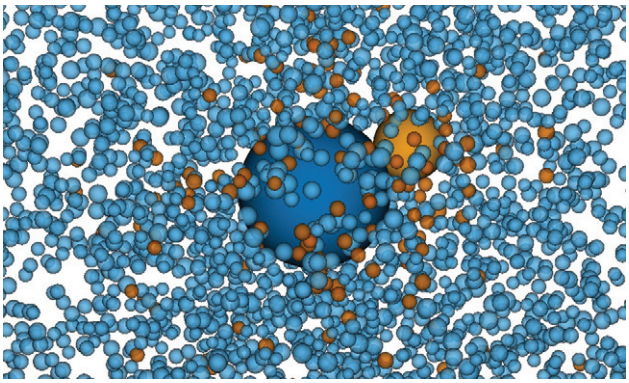

Fig. 1: (Colour on-line) Sphere dimer motor ($\sigma_{\mathrm{N}} = 10$), comprising C sphere (orange) and N sphere (blue), in solvent consisting of species A (sky blue) and B (vermilion). The solvent is shown with reduced density $0.04\sigma^{-3}$ instead of $0.8\sigma^{-3}$.

very small nanoscale environments. Recently, experiments have shown that single enzymes and small organometallic molecules undergoing catalytic activity exhibit enhanced diffusion in comparison to their inactive forms, and this enhancement has been attributed to propulsion on the molecular level [23–25]. Given this context, studies of the dynamics of small molecular-scale motors will contribute to the origins, characterization and consequences of directed motion in this regime.

We employ full molecular dynamics to study a simple model system made of a small sphere dimer motor [26], comprising linked catalytic and non-catalytic spheres, in a structureless solvent (see fig. 1). Chemical reactions at the catalytic sphere convert reactants to products. Due to the spatially asymmetric catalytic activity of the motor, an inhomogeneous distribution of these species is produced. This self-generated concentration gradient is an essential element that leads to propulsion in solution [9]. Micron-size sphere dimer motors comprising silica non-catalytic and Pt catalytic spheres have been studied experimentally [14]. While motor dynamics often takes place in aqueous solution, our structureless solvent model is sufficient to capture the important dynamical and structural effects that occur at the Ångström scale. Applications to specific systems should address effects related to the unique structural properties of water.

The system is contained in a cube of volume $V = (50\sigma)^3$ with periodic boundary conditions. The solvent consists of $N_{\mathrm{s}} = 10^5$ particles with number density $\varrho_{\mathrm{s}} = N_{\mathrm{s}}/V = 0.8\sigma^{-3}$ and two species, reactant (A) and product (B), both with diameter σ and mass m. The motor consists of rigidly linked catalytic (C) and non-catalytic (N) spheres with diameters $\sigma_{\mathrm{C}} = 2\sigma, \ldots, 5\sigma$ and $\sigma_{\mathrm{N}} = 4\sigma, \ldots, 10\sigma$, respectively, and neutrally buoyant mass $M_{\mathrm{m}} = \frac{\pi}{6}\varrho_{\mathrm{s}} m(\sigma_{\mathrm{C}}^3 + \sigma_{\mathrm{N}}^3)$. The separation of the spheres is chosen as[1] $R = \sqrt[6]{2}\,((\sigma_{\mathrm{C}} + \sigma_{\mathrm{N}})/2 + \sigma)$. The C sphere catalyses the chemical reaction[2] A $\rightarrow$ B, which occurs with unit probability when A comes within interaction range of C. All particles interact via the shifted, truncated Lennard-Jones potential, $V_{ij}(r) = \epsilon_{ij}(4((\sigma_{ij}/r)^{12} - (\sigma_{ij}/r)^6) + 1)$ for $r < \sqrt[6]{2}\sigma_{ij}$ and zero otherwise. Here r is the minimum image distance between the centres of a pair of particles, $\sigma_{\mathrm{CA}} = \sigma_{\mathrm{CB}} = \frac{1}{2}(\sigma_{\mathrm{C}} + \sigma)$ and $\sigma_{\mathrm{NA}} = \sigma_{\mathrm{NB}} = \frac{1}{2}(\sigma_{\mathrm{N}} + \sigma)$ for pairs of dimer sphere and solvent particle, and $\sigma_{\mathrm{AA}} = \sigma_{\mathrm{AB}} = \sigma_{\mathrm{BB}} = \sigma$ for pairs of solvent particles. The interaction energy is ϵ for all pairs apart from NB pairs, where $\epsilon_{\mathrm{NB}} = 0.1\epsilon, \ldots, 10\epsilon$. The temperature of the system is $k_{\mathrm{B}}T/\epsilon = 1$. The system is maintained in a non-equilibrium steady state by converting B particles back to A far from the dimer. Newton's equations of motion were solved[3] iteratively using the velocity-Verlet algorithm with $\delta t = 0.001\tau$.

Simulation results are reported in dimensionless units where distance is given in units of σ, mass in units of m, energy in units of ϵ, and time in units of $\tau = \sigma\sqrt{m\epsilon^{-1}}$. Our parameters are chosen to model a dense fluid argon-like solvent and, using argon [27] values of $\sigma = 0.34\,\mathrm{nm}$, $\epsilon = 120\,\mathrm{K}\,k_{\mathrm{B}}$, and $m = 39.95\,\mathrm{u}$ and $\tau = 2.15\,\mathrm{ps}$, we can assign physical values to our Ångström-scale motor simulations.

The non-equilibrium steady-state average velocity of the sphere dimer motor projected along its internuclear axis, $\langle V_z \rangle$, can be used to characterize the dynamics of the motor. Here $V_z = \hat{\mathbf{z}} \cdot \mathbf{v}_{\mathrm{cm}}$, with $\mathbf{v}_{\mathrm{cm}}$ the velocity of the centre of mass of the dimer and $\hat{\mathbf{z}}$ a unit vector along the bond (z-axis) directed from the N sphere to the C sphere. The average $\langle V_z \rangle$ and its fluctuations can be determined from the probability density, $f(V_z)$, which is shown in fig. 2 for two dimers with different sizes, $\sigma_{\mathrm{N}} = 10$ and $\sigma_{\mathrm{N}} = 4$, for several values of ϵ_{NB}. The figure plots the scaled velocity $V_z' = V_z\sqrt{M_{\mathrm{m}}/k_{\mathrm{B}}T}$ so that in scaled units the widths of the distributions are the same. These probability densities have a Maxwell-Boltzmann form, $f(V_z') = (2\pi)^{-1/2}\mathrm{e}^{-(V_z' - \langle V_z' \rangle)^2/2}$. The figure shows that the sphere dimer moves in the direction of the catalytic sphere (positive $\langle V_z' \rangle$) when $\epsilon_{\mathrm{NB}} < 1$ and in the opposite direction (negative $\langle V_z' \rangle$) when $\epsilon_{\mathrm{NB}} > 1$; when $\epsilon_{\mathrm{NB}} = 1$, $\langle V_z \rangle = 0$. The values of $\langle V_z' \rangle$ are given in table 1 for a variety of dimer sizes and potential parameters. As the dimer size decreases the propulsion speed is a smaller fraction of the mean thermal speed and the effects of fluctuations are felt more strongly.

The propulsion of the sphere dimer has its origin in the force on the dimer that arises from the different intermolecular potentials of the A and B particles with the dimer spheres and the self-generated non-equilibrium

[1] The choice of R conserves energy for the chemical reaction A $\rightarrow$ B in light of the differing ϵ_{NA} and ϵ_{NB}, by ensuring that a solvent particle A or B is within interaction range of at most a single dimer sphere, either C or N, at any given time.

[2] The reaction is diffusion-limited since $k = k_D k_0/(k_D + k_0) \simeq k_D$, where the reaction rate constant $k_0 = R_0^2\sqrt{8\pi k_{\mathrm{B}}T/m}$ is 8–16 times larger than the Smoluchowski rate constant $k_D = 4\pi D_{\mathrm{s}} R_0$ for $R_0 = 2^{1/6}(\sigma_{\mathrm{C}} + \sigma)/2$ and $D_{\mathrm{s}} = 0.086$.

[3] The simulations were performed on GPUs and CPUs using a self-written code in the programming languages OpenCL C and Lua to be published alongside a subsequent computational article.

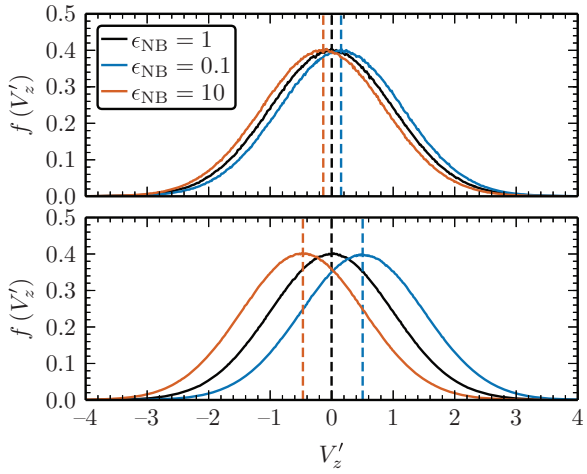

Fig. 2: (Colour on-line) Probability densities of the scaled propulsion velocity, $f(V_z')$, for small ($\sigma_N = 4$; top) and large ($\sigma_N = 10$; bottom) dimers, for several values of ϵ_{NB}. The dashed lines indicate the means, $\langle V_z' \rangle$, of the distributions.

Table 1: Sphere dimer properties for several diameters, σ_N and $\sigma_C = \sigma_N/2$, and values of ϵ_{NB}: Mean scaled propulsion velocity, $\langle V_z' \rangle$, orientational relaxation time, τ_r, diffusion constant, D_m, theoretical estimate for diffusion constant, D_m^{th}, scaled ballistic prefactor, $\mathcal{B}_I'$, and theoretical estimate for scaled ballistic prefactor, $\mathcal{B}_I'^{th}$.

σ_N	ϵ_{NB}	$\langle V_z' \rangle$	τ_r	D_m	D_m^{th}	$\mathcal{B}_I'$	$\mathcal{B}_I'^{th}$
10	1	−0.002	2035	0.006		2.977	
10	0.1	0.504	1931	0.361	0.352	3.265	3.254
10	10	−0.468	3774	0.659	0.590	3.196	3.219
8	1	0.001	1010	0.008		2.985	
8	0.1	0.365	1078	0.198	0.207	3.138	3.133
8	10	−0.345	2134	0.389	0.359	3.098	3.119
6	1	0.002	531	0.010		2.981	
6	0.1	0.254	503	0.109	0.117	3.062	3.065
6	10	−0.232	1036	0.207	0.192	3.025	3.054
4	1	0.001	195	0.018		2.952	
4	0.1	0.153	174	0.057	0.063	2.991	3.023
4	10	−0.137	302	0.110	0.080	2.963	3.019

inhomogeneous steady-state concentration fields. As a result the non-equilibrium average of the force projected along the dimer axis is $\langle \hat{\mathbf{z}} \cdot \mathbf{F}_m \rangle \neq 0$. Due to momentum conservation, this force can be written in terms of the force exerted on the solvent,

$$\langle \hat{\mathbf{z}} \cdot \mathbf{F}_m \rangle = \int d\mathbf{r} \varrho(\mathbf{r}) (\hat{\mathbf{z}} \cdot \hat{\mathbf{r}}) \frac{dV_{CA}(r)}{dr} + \sum_{\alpha=A}^{B} \int d\mathbf{r}' \varrho_\alpha(\mathbf{r}' + R\hat{\mathbf{z}}) (\hat{\mathbf{z}} \cdot \hat{\mathbf{r}}') \frac{dV_{N\alpha}(\mathbf{r}')}{dr'}, \quad (1)$$

where $\mathbf{r}$ has the catalytic C sphere as the origin, while $\mathbf{r}' = \mathbf{r} - R\hat{\mathbf{z}}$ is defined with the non-catalytic N sphere as the origin. In eq. (1) $\varrho_\alpha(\mathbf{r}) = \langle \varrho_\alpha(\mathbf{r}; \mathbf{r}^{N_\alpha}) \rangle$ is the non-equilibrium average of the microscopic concentration field, $\varrho_\alpha(\mathbf{r}; \mathbf{r}^{N_\alpha}) = \sum_{i=1}^{N_\alpha} \delta(\mathbf{r}_{i\alpha} - \mathbf{r})$. The total concentration of the A and B fields is $\varrho(\mathbf{r}) = \varrho_A(\mathbf{r}) + \varrho_B(\mathbf{r})$. In our simulations we have $V_{CA} = V_{CB}$ and have used this fact in writing the first term in eq. (1), which now depends only on the total concentration in the vicinity of the C sphere. Since $V_{NA} \neq V_{NB}$, the second term depends on the individual A and B concentration fields close to the N sphere and is the term that dominates the force.

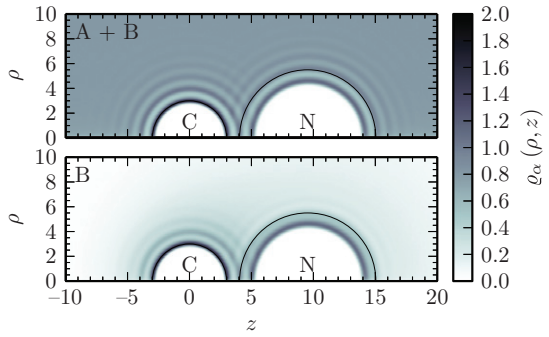

Fig. 3: (Colour on-line) Cylindrically averaged solvent density fields, $\varrho(\mathbf{r})$ (top) and $\varrho_B(\mathbf{r})$ (bottom), in the frame of the moving dimer, for the large dimer ($\sigma_N = 10$) and $\epsilon_{NB} = 0.1$. The solid black lines indicate the interaction distances $\sigma_{C\alpha}$ and $\sigma_{N\alpha}$.

The concentration fields are significantly influenced by solvent structural effects as can be seen in fig. 3, which shows $\varrho(\mathbf{r})$ and $\varrho_B(\mathbf{r})$ in a cylindrical coordinate frame (ρ, z, ϕ) that is co-moving with the dimer. The concentration fields exhibit oscillations near the surface of the dimer spheres that are characteristic of particles with an excluded volume. The radial (top) and angular (bottom) concentration fields with origin at the centre of the N sphere are shown in fig. 4. The radial concentration fields are determined by separately averaging over N hemispherical regions with $\hat{\mathbf{r}}' \cdot \hat{\mathbf{z}} > 0$ (towards the C sphere, solid lines) and $\hat{\mathbf{r}}' \cdot \hat{\mathbf{z}} < 0$ (away from the C sphere, dashed lines) in order to characterize the inhomogeneous nature of the concentration fields around the N sphere. Since the interaction potentials have finite range and are non-zero only for $r' < \sqrt[6]{2}\sigma_{N\alpha}$ (vertical dashed line in the figure), the density fields with values in this range contribute to the propulsion force; the system is force-free outside this boundary layer region. The pronounced oscillations in the radial concentration fields are evident within the boundary layer surrounding the dimer and directly affect the propulsion force in eq. (1). A major element in the force that drives propulsion is the concentration inhomogeneity across the N sphere and this is evident in the angular dependence of the concentration fields at a fixed value of r' shown in the lower panel of the figure. For θ values close to zero near the C sphere the B concentration is large and the A concentration is small. As θ increases to values near π on the opposite side of the N sphere the A concentration increases while B decreases.

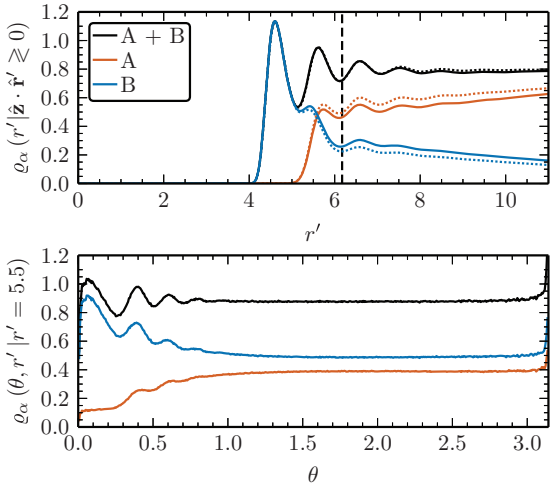

Fig. 4: (Colour on-line) Radial (top) and angular (bottom) solvent density, of species A, B, and both, from the centre of the N sphere, for the large dimer ($\sigma_\mathrm{N} = 10$) and $\epsilon_\mathrm{NB} = 0.1$. The radial density is averaged separately over each hemisphere: the solid lines show the density averaged over the hemisphere on the positive z-axis (towards the C sphere), the dashed lines over the hemisphere on the negative z-axis (away from the C sphere). The vertical dashed line indicates the cut-off distance of the force, $r_\mathrm{c} = \sqrt[6]{2}\,(\sigma_\mathrm{N}+1)/2$. The angular density is averaged over the azimuth angle, ϕ, at a distance $r' = 5.5$ from the centre of the N sphere, which corresponds to the second peak of the total radial density.

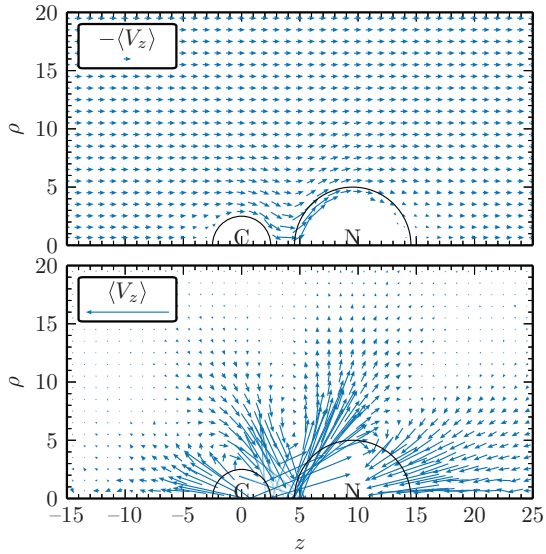

Fig. 5: (Colour on-line) Cylindrically averaged fluid velocity field, $\mathbf{v}(\rho, z)$, relative to the moving dimer, for the large dimer ($\sigma_\mathrm{N} = 10$) and $\epsilon_\mathrm{NB} = 0.1$. The fluid velocity field is shown in the dimer frame (top) and in the simulation frame (bottom).

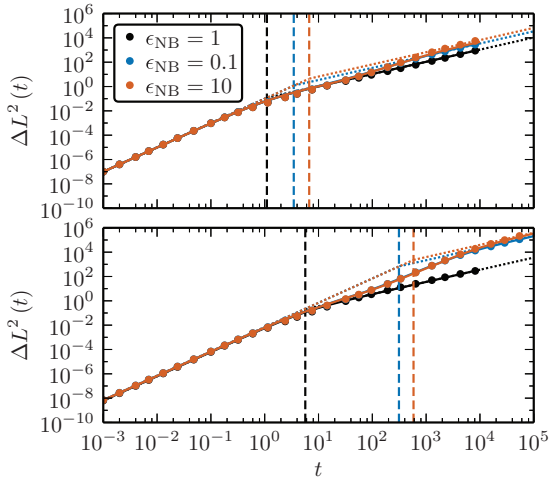

Fig. 6: (Colour on-line) Mean square displacement for small ($\sigma_\mathrm{N} = 4$; top) and large ($\sigma_\mathrm{N} = 10$; bottom) dimers, for several values of ϵ_NB. The dotted lines show fits of ballistic and diffusive regimes. The vertical dashed lines indicate crossover times, τ_c, between these regimes. The solid lines show theoretical estimates (eq. (4)).

Due to momentum conservation, fluid flows are generated in the solvent and are an integral part of the propulsion mechanism. On molecular scales continuum hydrodynamic approaches break down. However, such descriptions have proven to be successful on even very small scales. Similar observations apply to the flows generated by our Ångström-scale motors. Due to the small size of a motor and the strong thermal fluctuations it experiences, extensive averaging is required to visualize the fluid flow fields[4]. In fig. 5 the fluid velocity fields are shown in a cylindrical coordinate fame using two different representations. The top panel shows the flow field in a moving frame where the dimer velocity is zero. The flow field far from the dimer has the value $-\langle V_z\rangle$. The lower panel shows the flow field in the vicinity of the moving dimer. Here the flow field far from the dimer tends to zero while a flow field with dipole-like components exists in the vicinity of the dimer. These results are consistent with the macroscopic flows that appear in the phoretic mechanism for propulsion [28].

The mean square displacement (MSD) of the motor, $\Delta L^2(t) = \langle|\mathbf{r}_\mathrm{cm}(t) - \mathbf{r}_\mathrm{cm}(0)|^2\rangle$, where $\mathbf{r}_\mathrm{cm}$ is the position of the centre of mass of the dimer, is plotted in fig. 6 for chemically active dimers with different sizes, $\sigma_\mathrm{N} = 10$ and $\sigma_\mathrm{N} = 4$; the results for the corresponding chemically inactive dimers are also plotted for comparison. Both ballistic ($\sim \mathcal{B}_\mathrm{I} t^2$) and diffusive ($\sim 6D_\mathrm{m} t$) regimes, indicated by the straight lines, can be seen in the plots. The vertical dashed lines indicate the crossover times, τ_c, between these regimes. The prefactors $\mathcal{B}'_\mathrm{I} = \mathcal{B}_\mathrm{I} M_\mathrm{m}/k_\mathrm{B}T$ that characterize the ballistic regime and the dimer diffusion coefficients D_m, obtained from short- and long-time fits to the data, respectively, are given in table 1, along with several other quantities that are used in the analysis given below.

[4]The velocity fields are averaged over 1000 configurations per realization of 10^7 steps, and 100 realizations. The solvent velocities are transformed to the non-inertial dimer frame by $\mathbf{v}'_i = \mathbf{v}_i - \mathbf{v}_\mathrm{cm} - \boldsymbol{\omega}\times(\mathbf{r}_i - \mathbf{r}_\mathrm{cm})$, where ω is the angular velocity of the dimer.

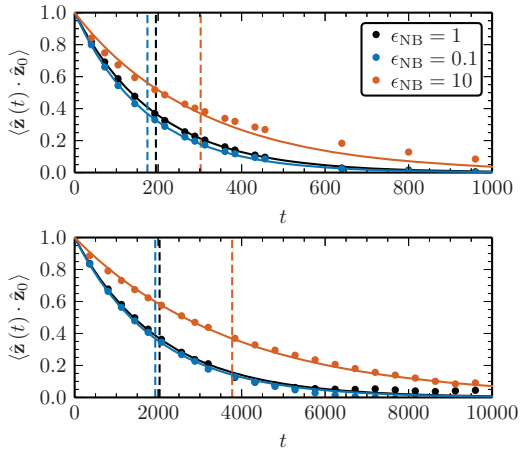

Fig. 7: (Colour on-line) Auto-correlation of orientation $\hat{\mathbf{z}}(t)$ for small ($\sigma_N = 4$; top) and large ($\sigma_N = 10$; bottom) dimers, for several values of ϵ_{NB}. The solid lines show a fit that assumes exponential decay. The vertical dashed lines indicate decay times τ_r.

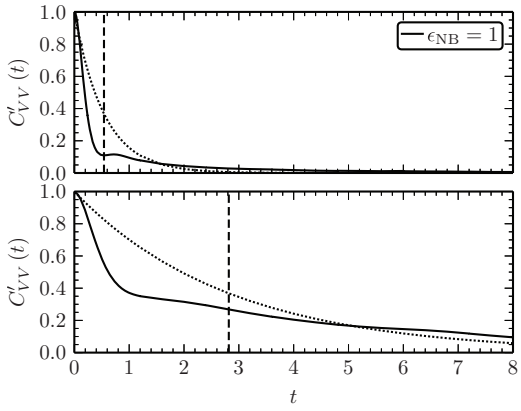

Fig. 8: Normalised auto-correlation of the velocity, $C'_{VV}(t) = C_{VV}(t)/(k_B T/M_m)$, for small ($\sigma_N = 4$; top) and large ($\sigma_N = 10$; bottom) dimers, for several values of ϵ_{NB}. The dotted lines show a fit of an exponential decay to the measured data. The vertical dashed lines indicate decay times τ_v.

The MSD can be written using the dimer velocity autocorrelation function (VAF), $C_{VV}(t) = \frac{1}{3}\langle \mathbf{V}(t) \cdot \mathbf{V} \rangle$, as

$$\Delta L^2(t) = \int_0^t \mathrm{d}t' \int_0^{t'} \mathrm{d}t'' C_{VV}(t''). \tag{2}$$

Expressing the velocity in terms of its average in the direction of the dimer axis and deviations from this value, $\mathbf{V}(t) = \langle V_z \rangle \hat{\mathbf{z}}(t) + \delta\mathbf{V}(t)$, inserting this expression in the definition of the VAF, and assuming exponential decay of the orientation, $\langle \hat{\mathbf{z}}(t) \cdot \hat{\mathbf{z}} \rangle = \mathrm{e}^{-t/\tau_r}$, and velocity, $\langle \delta\mathbf{V}(t) \cdot \delta\mathbf{V} \rangle = (3k_B T/M_m)\mathrm{e}^{-t/\tau_V}$, correlation functions we obtain,

$$C_{VV}(t) = \frac{1}{3}\langle V_z \rangle^2 \mathrm{e}^{-t/\tau_r} + \frac{k_B T}{M_m}\mathrm{e}^{-t/\tau_v}. \tag{3}$$

Using this expression, the MSD takes the form

$$\Delta L^2(t) = 6D_m t - 2\langle V_z \rangle^2 \tau_r^2 \left(1 - \mathrm{e}^{-t/\tau_r}\right) - 6\frac{k_B T}{M_m}\tau_v^2 \left(1 - \mathrm{e}^{-t/\tau_v}\right). \tag{4}$$

In the ballistic regime, $t \ll \tau_v$, the MSD reduces to $\Delta L^2(t) \approx (3k_B T/M_m + \langle V_z \rangle^2)t^2 = \mathcal{B}_I t^2$, while in the diffusive regime, $t \gg \tau_r$, we have $\Delta L^2(t) \approx 6((k_B T/M_m)\tau_v + \frac{1}{3}\langle V_z \rangle^2 \tau_r)t = 6D_m t$. The effective dimer diffusion coefficient is $D_m = D_0 + \frac{1}{3}\langle V_z \rangle^2 \tau_r$. The diffusion coefficient in the absence of propulsion is $D_0 = (k_B T/M_m)\tau_v$.

The assumptions made in constructing this model for the VAF and MSD can be tested by direct simulation. The orientational correlation function is plotted in fig. 7 for dimers with $\sigma_N = 10$ and 4 for three values of ϵ_{NB}. The correlation function decay is well approximated by an exponential form and the orientational relaxation time τ_r can be determined. Note the significant difference in the orientational relaxation times between the $\epsilon_{NB} = 0.1$ and $\epsilon_{NB} = 1$ cases, which are the same within statistical errors, and the $\epsilon_{NB} = 10$ case where τ_r is significantly longer. In this latter case, since $\epsilon_{NB} \gg \epsilon_{NA}$, the B particles interact with the N sphere with a repulsive potential that is much stronger than the A–N repulsive potential. This results in propulsion with the N sphere in front (negative velocity) and motion down the concentration gradient, which tends to stabilize the motor to orientational fluctuations. Such effects have been considered for pushers and pullers for motors with dimer geometries [29]. The τ_r relaxation times for a variety of parameters are presented in table 1.

The VAFs for an inactive dimer ($\langle V_z \rangle = 0$) are presented in fig. 8. These correlation functions cannot be quantitatively modelled by exponential decay and show additional structure. As expected for systems with continuous potentials there is a very small inertial regime where the VAF behaves as $\sim \langle V(0)^2 \rangle - \langle F(0)^2 \rangle/(2M_m^2)t^2$, and gives rise to a zero initial slope. Here $F(0)$ is the initial value of the force on the dimer. This regime has negligible consequence for our low Reynolds number conditions. The VAF exhibits other characteristic features. For the small dimer with $\sigma_N = 4$ a minimum in the decay is clearly seen and is due to caging effects that are significant when the dimer is comparable in size to the solvent. For the larger dimer this effect is smaller and no minimum is seen. For both dimer sizes there is a long-time power law decay due to the coupling of solvent collective modes to the dimer centre-of-mass velocity. The long-time decay is especially evident for the larger dimer.

The simulation results can now be compared with the theoretical expression in eq. (4) and its limits in the ballistic and diffusive regimes. In the ballistic regime we have $\mathcal{B}'_I = 3 + \langle V'_z \rangle^2$. Table 1 shows that the ballistic regime is dominated by thermal speed $3k_B T/M_m$ ($\mathcal{B}'_I \simeq 3$), rather than the square of the propulsion velocity as is the case for micron-scale motors. This is one of the signatures that distinguish the behaviour of Ångström-scale motors from

their larger counterparts. The effects of self-propulsion manifest themselves clearly when the long-time diffusive regime is examined. The diffusion coefficient D_{m} obtained from the MSD and its theoretical estimate $D_{\mathrm{m}}^{\mathrm{th}}$ are in close accord. When $\epsilon_{\mathrm{NB}} = 1$ there is no propulsion and the diffusion coefficient is given by D_0. Propulsion contributes significantly to the magnitude of the diffusion coefficient and D_{m} is 50–100 times larger than D_0 for the large motor and 3–9 times larger for the small motor. The full expression for $\Delta L^2(t)$ in eq. (4) agrees well with the simulation data (fig. 6); the small deviations can be attributed to the approximation that the VAF decays exponentially.

Converted to physical units, the large motor with length $(\sigma_{\mathrm{C}} + \sigma_{\mathrm{N}})/2 + R = 5.79\,\mathrm{nm}$ is propelled with velocity $\langle V_z \rangle = 3.67\,\mathrm{nm\,ns^{-1}}$, for $\epsilon_{\mathrm{NB}} = 0.1$. For $\tau_{\mathrm{r}} = 4.15\,\mathrm{ns}$ it travels an average distance $\langle V_z \rangle \tau_{\mathrm{r}} = 15.23\,\mathrm{nm}$, or 2.63 times its length. The small motor with length 2.55 nm is propelled with velocity $4.40\,\mathrm{nm\,ns^{-1}}$. For 0.37 ns it travels an average distance 1.65 nm, or 0.65 times its length.

The results reported here show that Ångström-scale chemically powered motors operate in a strongly fluctuating medium where the ballistic regime is dominated by the thermal speed rather than the propulsion speed. Nevertheless, self-propulsion is responsible for the very large enhancements of the motor diffusion coefficients. The motors are driven by the microscopic analogues of phoretic mechanisms and, after substantial averaging to remove the effects of fluctuations, one can observe the solvent flow fields that are an integral part of the propulsion mechanism. From the above discussion we see that these motors operate in nanometre and nanosecond regimes. Although the average motor velocities are very large, the reorientation times are very short. The results suggest that such very small motors could have applications in nanoscale systems that make use of the fast motor diffusion and the solvent velocity fields generated by the motor motion. If the motion of the motors is constrained so that orientational relaxation is hindered, their directed motion could be exploited to achieve targeted delivery or active transport on nanoscale, very much like biological machines.

* * *

Part of this work was supported by a grant from Natural Sciences and Engineering Research Council of Canada.

REFERENCES

[1] Alberts B., Bray D., Lewis J., Raff M., Roberts K. and Watson J. D., *Molecular Biology of the Cell*, 3rd edition (Garland Science) 2002.

[2] Pei R., Taylor S. K., Stefanovic D., Rudchenko S., Mitchell T. E. and Stojanovic M. N., *J. Am. Chem. Soc.*, **128** (2006) 12693.

[3] Yin P., Choi H. M. T., Calvert C. R. and Pierce N. A., *Nature*, **451** (2008) 318.

[4] Omabegho T., Sha R. and Seeman N. C., *Science*, **324** (2009) 67.

[5] Purcell E. M., *Am. J. Phys.*, **45** (1977) 3.

[6] Hong Y., Velegol D., Chaturvedi N. and Sen A., *Phys. Chem. Chem. Phys.*, **12** (2010) 1423.

[7] Mirkovic T., Zacharia N. S., Scholes G. D. and Ozin G. A., *ACS Nano*, **4** (2010) 1782.

[8] Wang J., *ACS Nano*, **3** (2009) 4.

[9] Kapral R., *J. Chem. Phys.*, **138** (2013) 020901.

[10] Paxton W. F., Kistler K. C., Olmeda C. C., Sen A., St. Angelo S. K., Cao Y., Mallouk T. E., Lammert P. E. and Crespi V. H., *J. Am. Chem. Soc.*, **126** (2004) 13424.

[11] Zacharia N. S., Sadeq Z. S. and Ozin G. A., *Chem. Commun.* (2009) 5856.

[12] Ebbens S., Tu M.-H., Howse J. R. and Golestanian R., *Phys. Rev. E*, **85** (2012) 020401.

[13] Baraban L., Tasinkevych M., Popescu M. N., Sanchez S., Dietrich S. and Schmidt O. G., *Soft Matter*, **8** (2012) 48.

[14] Valadares L. F., Tao Y.-G., Zacharia N. S., Kitaev V., Galembeck F., Kapral R. and Ozin G. A., *Small*, **6** (2010) 565.

[15] Anderson J. L. and Prieve D. C., *Sep. Purif. Rev.*, **13** (1984) 67.

[16] Anderson J. L. and Prieve D. C., *Langmuir*, **7** (1991) 403.

[17] Fair M. and Anderson J., *J. Colloid Interface Sci.*, **127** (1989) 388.

[18] Golestanian R., Liverpool T. B. and Ajdari A., *Phys. Rev. Lett.*, **94** (2005) 220801.

[19] Jülicher F. and Prost J., *Eur. Phys. J.*, **29** (2009) 27.

[20] Popescu M. N., Dietrich S., Tasinkevych M. and Ralston J., *Eur. Phys. J. E*, **31** (2010) 351.

[21] Sabass B. and Seifert U., *J. Chem. Phys.*, **136** (2012) 064508.

[22] Alder B. J. and Wainwright T. E., *Phys. Rev. A*, **1** (1967) 18.

[23] Muddana H. S., Sengupta S., Mallouk T. E., Sen A. and Butler P. J., *J. Am. Chem. Soc.*, **132** (2010) 2110.

[24] Sengupta S., Dey K. K., Muddana H. S., Tabouillot T., Ibele M. E., Butler P. J. and Sen A., *J. Am. Chem. Soc.*, **135** (2013) 1406.

[25] Pavlick R. A., Dey K. K., Sirjoosingh A., Benesi A. and Sen A., *Nanoscale*, **5** (2013) 1301.

[26] Rückner G. and Kapral R., *Phys. Rev. Lett.*, **98** (2007) 150603.

[27] Rahman A., *Phys. Rev.*, **136** (1964) A405.

[28] Anderson J. L., *Phys. Fluids*, **26** (1983) 2871.

[29] Popescu M. N., Tasinkevych M. and Dietrich S., *EPL*, **95** (2011) 28004.